Research Square

Preprints are preliminary reports that have not undergone peer review.
They should not be considered conclusive, used to inform clinical practice,
or referenced by the media as validated information.

Modeling and Simulation of Magnetized Casson–Micropolar Hybrid Nanofluid Due to Curved Surface with Viscous Dissipation and Thermal Slip Effects

Iskander Tlili
Islamic University of Madinah
S. Anitha
anitha@psgitech.ac.in

PSG Institute of Technology and Applied Research
K Nagegowda
Davangere University
U. S. Mahabaleshwar
Davangere University
Ravikumar Jayabal
AMET University
K Logesh
Vel Tech Rangarajan Dr. Sagunthala R&D Institute of Science and Technology

Research Article

Keywords: Hybrid nanofluid, Curved surface, Viscous dissipation, heat source, Thermal slip, heat transfer management

Posted Date: August 3rd, 2026

DOI: https://doi.org/10.21203/rs.3.rs-10338134/v1

License: This work is licensed under a Creative Commons Attribution 4.0 International License.
Read Full License

Additional Declarations: No competing interests reported.

Modeling and Simulation of Magnetized Casson–Micropolar Hybrid Nanofluid Due to Curved Surface with Viscous Dissipation and Thermal Slip Effects

Iskander Tlili[1], S. Anitha[2, *], Nagegowda K[3], U. S. Mahabaleshwar[3], Ravikumar Jayabal[4] and K Logesh[5]

[1]Department of Mechanical Engineering, Faculty of Engineering, Islamic University of Madinah, Madinah 42351, Saudi Arabia

[2] Department of Mathematics, PSG Institute of Technology and Applied Research, Coimbatore, Tamil Nadu, INDIA.

[3]Department of Studies in Mathematics, Davangere University, Shivagangothri, Davangere, 577 007, India.

[4]Department of Mechanical Engineering, Academy of Maritime Education and Training, AMET University, Kanathur, Chennai, Tamil Nadu, India.

[5]Department of Mechanical Engineering, Vel Tech Rangarajan Dr. Sagunthala R&D Institute of Science and Technology, Chennai, India.

*Corresponding author: anitha@psgitech.ac.in

Author's Email:

itlili@iu.edu.sa , anitha@psgitech.ac.in , nagegowda.k04@gmail.com,

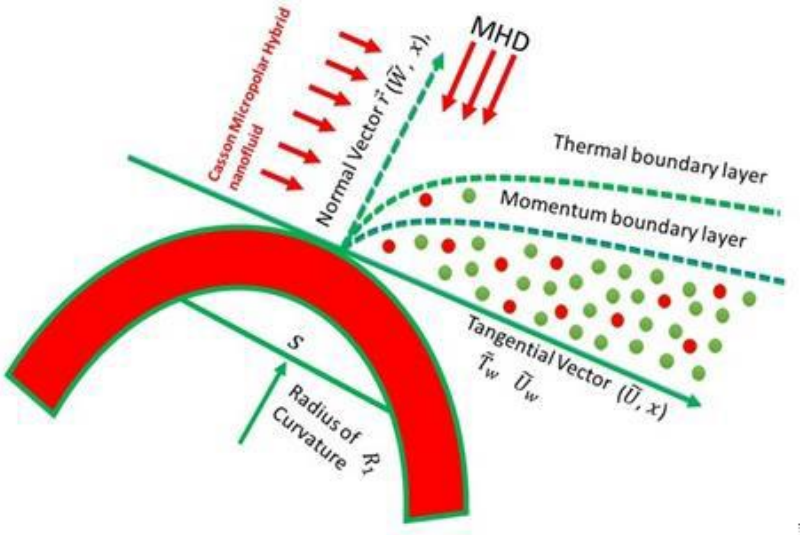
u.s.m@davangereuniversity.ac.in , drravikumarjayabal@gmail.com , klogesh7@gmail.com

Abstract:

This study investigates the magnetized Casson–micropolar hybrid nanofluid flow over a curved elastic surface considering viscous dissipation and thermal slip effects. The hybrid nanofluid is formed by dispersing silver (Ag) and titanium oxide (TiO_2) nanoparticles in hexanol base fluid to enhance thermal

transport. The governing nonlinear equations for momentum, microrotation, and heat transfer are transformed into dimensionless form and solved numerically using the shooting method with Runge–Kutta integration. Results show that increasing the Hartmann number from 0 to 1 reduces velocity by nearly 25–30%, while the Casson parameter increases temperature by 12–16%. The Eckert number enhances temperature by 15–20%, and the heat source parameter increases thermal distribution by 20–25%. The hybrid nanofluid demonstrates superior heat transfer compared to mono nanofluid systems.

Keywords: *Hybrid nanofluid; Curved surface; Viscous dissipation; heat source; Thermal slip; heat transfer management.*



Graphical abstract

1. Introduction

The nanofluids present distinct combination of impressive thermal conductivity, enhanced convective heat transfer, tunable features, updated rheology and significant interfacial behavior. Such extensive properties originate from the nanoscale features of particles, involving high surface area, peak particles

interaction and Brownian diffusion. Subject to these aspects, these materials have potential to revolutionize heat transfer management and energy systems, enhancing the cooling and heating solution which cannot be maintain through traditional base fluids. With versatile thermal nature and adaptability, the nanomaterials show innovation across various engineering and industrial domain. Parmar et al. [1] characterized thermal features of nanofluid comprising the entropy generation in porous closure. Rajput et al. [2] focused to dynamic and consequences of heat transfer due to nanofluid by using the Buongiorno fluid modelling. Nagaraja et al. [3] expressed the inertial mechanism while focusing the heat transfer enhancement due to nanofluid in curved configuration. Thermal discussion of carbon nanotubes in expanding surface by accounting the multiple features was analyzed by Rajput et al. [4]. Mekheimer et al. [5] proposed role of electro-kinetic forces in thermal description of Maxwell nanofluid. Balamurugan and Chamkha [6] intended the quadratic nanofluid flow in slip regime additionally influenced with dissipation features. Sneha et al. [7] explored the influence of magnetic field and radiation Jeffery fluid flow on expanding/shrinking sheet with nanoparticles comprising carbon nanotubes. Nihaal et al. [8] investigated the consequences of viscous dissipation, joule heating, and activation energy on ternary nanofluid over three different surfaces. The features of permeability and chemical diffusion in magneto-driven flow of nanofluid has been focused by Goud and Reddy [9]. Sheikholeslami [10] identified the thermal innovation of hybrid nanofluid (HNF) and responded significance to solar systems.

Hybrid nanomaterials featured the growing category of engineering materials where two or more nanoparticles are dispersed in base fluid, providing enhanced physical and thermal features. Recent trends in thermal engineering proposed optimized combination of nanoparticles to achieve the peaked thermal conductivity, reduced viscosity and improved stability, enabling more effective thermal systems. Modern synthesis techniques like surface functionalization, ultrasonic dispersion and green chemistry routes are enhancing the particles stability and preventing agglomeration. The hybrid nanomaterials are widely used

in solar thermal collectors, automobile industries for cooling purpose, energy storage units, industrial heat exchangers, where enhanced heat transfer can lead to minimize the size and reduce the energy consumptions. Furthermore, hybrid nanomaterials preserve multi-scale emerging applications in advanced regression systems, microchannel cooling and biomedical devices, where the tunable features offer tailored thermal management for next-generation thermal systems. Nihaal et al. [10] examined the impact of heat source/sink on non-Newtonian hybrid nanofluid flow over a porous expanding surface. Hayat et al. [12] contributed to HNF analysis with entropy production and inertial features. Rafique et al. [13] investigated the tetra HNF inclined cylinder with quadratic radiation. Study of dusty HNF with joint features of Lorentz force has been characterized by Khan et al. [14]. Venkateswarlu et al. [15] observed the HNF features by accounting the electromagnetic force effects. Prediction of heat transfer through HNF trnaport in wavy surface was referred to analysis of Oudina et al. [16]. Bartwal et al. [17] justified the ternary hybrid nanoparticles features in rotatory regime with help of AI model. Alnahdi et al. [18] studied drug delivery applications subject to ternary HNF in capillary regime. Ahmad et al. [19] accounted the HNF transport in presence of microorganisms. Pattnaik et al. [20] determined the buoyancy driven flow of hybrid nanofluid with slip effects. Features of graphene and aluminum suspension with water by using the non-Fourier's modeling has been revealed by Rani et al. [21]. Thirunananasambantham et al. [22] considered the GPL blood suspension in stenosed arteries with magnetic features. Pai et al. [23] discovered hexanol base fluid features with inclusion of silica and titanium oxide nanoparticles.

Subject to increasing demand of peak performance thermal transport of fluids in modern energy and industrial systems, current analysis incorporates the magnetized flow and heat transfer features of Casson-Micropolar hybrid nanofluid due to curved surface with presence of variable thermal conductivity. The decomposition of hybrid nanofluid (HNF) is decomposed by dispersion of silver (Ag)

and titanium oxide nanoparticles (TiO_2) to improve thermal aspects of hexanol base fluid. The motivations for choice of such suspension are subject to synergistic improvement of thermal concavity and rheological behavior. The fluid is considered to be non-Newtonian Casson behavior with micropolar features, thereby accounting for micro-rotation, yield stress and particles couple stresses which are prominent in various complex fluids. The flow model comprises the viscous dissipation and additional heat source, which are essential in description of thermal processes in peak thermal management systems and high-shear environments. The thermal slip constraints are used near the curved surface to simulate the microscale heat features that rises in coated or insulated surfaces. The problem is solved with shooting numerical approach. Comparative discussion of thermal behavior of mono nanofluid and hybrid nanofluid is presented.

Novelty and Contributions:

Despite extensive research on nanofluids and hybrid nanofluids, the simultaneous consideration of Casson rheology, micropolar characteristics, curved surface geometry, magnetic field effects, viscous dissipation, and thermal slip boundary conditions in a unified framework remains largely unexplored. The present study addresses this gap and makes the following novel contributions:

1. First comprehensive model combining Casson-micropolar rheology with hybrid nanofluid: This study is among the first to simultaneously incorporate both Casson fluid yield stress behavior and micropolar microrotation effects in a hybrid nanofluid system, capturing the complex non-Newtonian characteristics relevant to biological fluids, polymer solutions, and advanced coolants.

2. Curved surface geometry with magnetic field: The analysis extends beyond flat plate configurations to investigate flow over curved elastic surfaces under magnetic field influence, which is critical for

applications in curved heat exchangers, biomedical devices with curved geometries, and electromagnetic flow control systems.

3. Comprehensive thermal effects: The model uniquely integrates viscous dissipation, variable thermal conductivity, heat source/sink, and thermal slip boundary conditions, providing a realistic representation of high-temperature and high-shear thermal management systems.

4. Ag-TiO_2/hexanol hybrid nanofluid system: The specific combination of silver and titanium oxide nanoparticles in hexanol base fluid has not been previously investigated for Casson-micropolar flow over curved surfaces, offering new insights for thermal system design with this promising nanofluid combination.

5. Rigorous validation framework: A comprehensive three-stage validation protocol is established, comparing results against multiple benchmark solutions for Casson fluids, micropolar fluids, and curved surface flows, ensuring high confidence in the numerical predictions.

These contributions advance the fundamental understanding of complex nanofluid flows and provide valuable design guidelines for next-generation thermal management systems in solar collectors, biomedical devices, electromagnetic cooling systems, and advanced heat exchangers.

2. Mathematical formulation

A laminar and steady Casson-micropolar hybrid nanofluid is taken into account due to curved elastic surface. The radial axis is defined by x, R_1 be curvature while surface arc length is denoted by S. Velocity components along arc length is defined by W while U is taken along radial direction. Magnetic features are normally assumed. Let N symbolizing the micro-rotation component, T_w is surface temperature, surface wall velocity is illustrated by U_w T_∞ is the ambient temperature. For analyzing heat transfer, the viscous dissipation and heat source relations are adopted in energy equation. Under such assumptions,

the problem is illustrated by following equations:

$$\frac{1}{x+R_1}((x+R_1)V)_r + \frac{R_1}{x+R_1}(U)_s = 0, \tag{1}$$

$$\frac{U^2}{x+R_1} = \frac{1}{\rho_{hnf}}P_r, \tag{2}$$

$$V(U)_r + \frac{R_1 U}{r+R_1}(U)_s + \frac{UV}{r+R_1} + \frac{1}{\rho_{hnf}}\frac{R_1}{r+R_1}P_s = \upsilon_{hnf}\left[\left(1+\frac{1}{\kappa}+k^*\right)\left(U_{rr} - \frac{U}{(r+R_1)^2} + \frac{1}{r+R_1}U_r\right)\right] - \frac{k^*}{\rho_{hnf}}(N)_r - \frac{\sigma_{hnf}{B_0}^2}{\rho_{hnf}}U, \tag{3}$$

$$V(N)_r + \frac{R_1 U}{r+R_1}(N)_s = \frac{\gamma_{hnf}}{\rho_{hnf} j}\left(N_{rr} + \frac{1}{r+R_1}N_r\right) - \frac{k^*}{\rho_{hnf} j}(2N + U_r + \frac{U}{r+R_1}), \tag{4}$$

$$V(T)_r + \frac{R_1 U}{r+R_1}(T)_s = \frac{1}{(\rho C_p)_{hnf}}\frac{1}{r+R_1}\left((r+R_1)T_r k_{hnf}(T)\right)_r + \frac{\mu_{hnf}}{(\rho C_p)_{hnf}}\left(1+\frac{1}{\beta}\right)\left(U_r + \frac{U}{r+R_1}\right)^2 + \frac{Q}{(\rho C_p)_{hnf}}(T - T_\infty), \tag{5}$$

Subject to:

$$U = U_w,\ V = 0,\ T = T_w + \chi_1\frac{k_{hnf}}{k_f}(T)_r,\ N = -n(U)_r \quad at\ r \to 0,$$
$$U = 0,\ T = T_\infty, \qquad N = 0, \qquad at\ r \to \infty. \tag{6}$$

with specific heat $(\rho C_p)_{hnf}$, vertex viscosity k^*, Casson fluid coefficient β, HNF density ρ_{hnf}, magnetic field strength, B_0, thermal conductivity k_{hnf}, electrical conductivity σ_{hnf}. Table 1 expresses mathematical modelling of problem.

Rotating gradient viscosity γ_{hnf} for micropolar fluid is:

$$\gamma_{hnf} = \left(\mu_{hnf} + \frac{k_1}{2}\right)j. \tag{7}$$

where j be micro-inertia. Following new variables are defined for simplifying the system:

Defining the dimensionless variables as:

$$T = T_\infty + e^{\frac{s}{a^*}}(T_w - T_\infty)\theta(\eta),\ \ \eta = r\sqrt{\frac{b^* e^{\frac{s}{a^*}}}{2\nu_f a^*}}, \qquad P = \rho_f {b^*}^2 e^{\frac{2s}{a^*}} p(\eta), \qquad N = b^* e^{\frac{3s}{2a^*}}\sqrt{\frac{b^*}{2\nu_f a^*}}\ g(\eta),$$

$$U = b^* e^{\frac{s}{a^*}} f'(\eta), \tag{8}$$

$$p' = \frac{(f')^2}{\eta+K} \tag{9}$$

Following system of equation is developed:

$$\frac{\eta K}{\eta+K}p' + \frac{4K}{\eta+K}p = \frac{\rho_f}{\rho_{hnf}}\left(\frac{1}{(1-\phi_1)^{2.5}(1-\phi_2)^{2.5}} + k_1 + \frac{1}{\kappa}\right)\left(f''' + \frac{1}{\eta+K}f'' - \frac{1}{(\eta+K)^2}f'\right) + \frac{K}{\eta+K}\left(ff'' + 2f'^2\right) -$$

$$\frac{K}{(\eta+K)^2}\left(ff' + \zeta f'^2\right) - k_1 g' - \frac{\sigma_{hnf}}{\sigma_f}Mf', \tag{10}$$

$$\frac{\rho_f}{\rho_{hnf}}\left(\frac{1}{(1-\phi_1)^{2.5}(1-\phi_2)^{2.5}} + \frac{k_1}{2}\right)\left(g'' + \frac{1}{\eta+K}g'\right) - k_1\left(2g + f'' + \frac{1}{\eta+K}f'\right) + \frac{K}{\zeta+K}gf' - \frac{K}{\eta+K}fg' = 0, \tag{11}$$

$$\frac{k_{hnf}}{k_f}\frac{(\rho C_p)_f}{(\rho C_p)_{hnf}}\frac{1}{P_r}(1+\beta\theta)\left(\frac{1}{\eta+K}\theta' + \theta''\right) + \beta\theta'^2 + \left(\frac{K}{\eta+K}f\theta' - \frac{K}{\zeta+K}2\theta f'\right) + \frac{\rho_f}{\rho_{hnf}}\frac{\mu_{hnf}}{\mu_f}E_c\left(1 + \frac{k_1}{2} +\right.$$

$$\left.\frac{1}{\beta}\right)\left[f'' - \frac{1}{\eta+K}f'\right]^2 + 2\delta\theta = 0, \tag{12}$$

$$\left.\begin{aligned} f(0) = 0, \quad f'(0) = 1, \quad \theta(0) = 1 + S\frac{k_{hnf}}{k_f}\theta'(0), \quad g(0) = -nf''(0), \\ f(\infty) \to 0 \quad , \quad g'(\infty) \to 1 \quad , \quad \theta(\infty) \to 0 \quad , \quad f''(\infty) \to 0. \end{aligned}\right\} \tag{13}$$

where $Pr = \frac{\nu_f}{\alpha}, Ec = \frac{{U_w}^2}{\nu_f c_p}, \delta = \frac{Q}{b^*\rho c_p}$ are Prandtl number, Eckert parameter and heat source constant, respectively.

The pressure gradient is eliminated which leads to following equations:

$$\frac{\rho_f}{\rho_{hnf}}\left(\frac{1}{(1-\phi_1)^{2.5}(1-\phi_2)^{2.5}} + \gamma + \frac{1}{\kappa}\right)\left(f^{iv} - \frac{1}{(\eta+\alpha)^2}f'' + \frac{1}{(\eta+\alpha)^3}f' + \frac{2}{\eta+\alpha}f'''\right) + \frac{\alpha}{\eta+\alpha}[ff'''] +$$

$$\frac{\alpha}{(\eta+\alpha)^3}[f'f + 2\eta(f')^2] - \frac{3\alpha}{\eta+\alpha}[f''f'] - \frac{\alpha}{(\eta+\alpha)^2}[f''f + 7(f')^2 + 4\eta f''f'] + \gamma g'' - \frac{\sigma_{hnf}}{\sigma_f}M\left[\frac{1}{\eta+\alpha}f' +\right.$$

$$f''\Big] = 0, \tag{14}$$

$$\frac{\rho_f}{\rho_{hnf}}\left(\frac{1}{(1-\phi_1)^{2.5}(1-\phi_2)^{2.5}}+\frac{\gamma}{2}\right)\left(g''+\frac{1}{\eta+\alpha}g'\right)-\gamma\left(2g+f''+\frac{1}{\eta+\alpha}f'\right)+\frac{\alpha}{\eta+\alpha}gf'-\frac{\alpha}{\eta+\alpha}fg'=0, \tag{15}$$

$$\frac{k_{hnf}}{k_f}\frac{(\rho C_p)_f}{(\rho C_p)_{hnf}}\frac{1}{P_r}(1+\beta\theta)\left(\frac{1}{\eta+\alpha}\theta'+\theta''\right)+\beta\theta'^2+\left(\frac{\alpha}{\eta+\alpha}f\theta'-\frac{\alpha}{\eta+\alpha}2\theta f'\right)=0. \tag{16}$$

Wall shear force and Nusselt number are:

$$C_f=\frac{\tau_{rs}}{\rho_{hnf}U_w^2}, \tau_{rs}=\left\{\frac{\rho_f}{\rho_{hnf}}\left(\frac{1}{(1-\phi_1)^{2.5}(1-\phi_2)^{2.5}}+\gamma+\frac{1}{\kappa}\right)\left(U_r+\frac{U}{r+R_1}\right)+k^*N\right\}_{r=0}, C_m=\frac{a^*e^{\frac{s}{a^*}}\tau_m}{\rho_{hnf}U_w^2},\ Nu=$$

$$\frac{sq_w}{k_f(T_w-T_\infty)}, q_w=-k_{hnf}(\mathrm{T})_{r_{r=0}}, \tau_m=\left\{\frac{\rho_f}{\rho_{hnf}}\left(\frac{1}{(1-\phi_1)^{2.5}(1-\phi_2)^{2.5}}+\frac{\gamma}{2}\right)\left(N_r+\frac{N}{r+R_1}\right)\right\}_{r=0}\Bigg\} \tag{17}$$

$$C_fRe_x^{1/2}=\frac{\rho_f}{\rho_{hnf}}\left(\frac{1}{(1-\phi_1)^{2.5}(1-\phi_2)^{2.5}}+\gamma+\frac{1}{\kappa}\right)\left(f''(0)+\frac{f'(0)}{\alpha}-n\gamma f''(0)\right), \tag{18}$$

$$C_mRe_x^{1/2}=\frac{\rho_f}{\rho_{hnf}}\left(\frac{1}{(1-\phi_1)^{2.5}(1-\phi_2)^{2.5}}+\frac{k_1}{2}\right)\left(g'(0)-\frac{nf''(0)}{\alpha}\right), \tag{19}$$

$$Nu\ Re_x^{1/2}=-\frac{k_{hnf}}{k_f}\theta'(0). \tag{20}$$

The mathematical expressions are defined in table 1 for features of HNF. Table 2 reports the range of numerical values of nanoparticles and base fluid.

Table 1: Mathematical relevance of HNF for different thermal features.

Properties	Hybrid Nano fluid
Density	$\frac{\rho_{hnf}}{\rho_f}=\phi_1\rho_{S_1}+(1-\phi_1).(1-\phi_2)\phi_2\rho_{S_2}$.
Heat capacity	$\frac{(\rho C_p)_{hnf}}{(\rho C_p)_f}=\phi_1(\rho C_p)_{S_1}+(1-\phi_1)(1-\phi_2)\phi_2(\rho C_p)_{S_2}$
Dynamics Viscosity	$\mu_{hnf}=\frac{\mu_f}{(1-\phi_1)^{2.5}(1-\phi_2)^{2.5}}$.
Thermal	

Conductivity	$\frac{k_{hnf}}{k_{bf}} = \frac{k_{s_2} + (n-1)k_{bf} - (k_{bf} - k_{s_2})(n-1)\phi_2}{k_{s_2} + (n-1)k_{bf} + (k_{bf} - k_{s_2})\phi_2}$
	$\frac{k_{bf}}{k_f} = \frac{k_{s_1} + (n-1)k_f - (k_f - k_{s_1})(n-1)\phi_1}{k_{s_1} + (n-1)k_f + (k_f - k_{s_1})\phi_1}$

Table 2: Numerical arrangement of nanoparticles (Au, Ag, TiO_2) and base fluid (hexanol) [22, 23].

Quantities	$\rho(kg/m^3)$	$k(W/mk)$	$C_p(J/kgK)$
Hexanol	815	0.15-0.2	2384
Au	19300	310	129
Ag	10500	429	235
TiO_2	4250	8.9	686.2

3. Methodology

Numerical findings are proposed for formulated problem via effective shooting technique. Due to excellence convergence and accuracy, the shooting scheme is most effective numerical tool for simulating the governing equations from complex systems. To convert the system into first order, following variables are suggested:

$$\Omega(1) = f(\zeta)\ ,\ \Omega(2) = f'(\zeta)\ , \Omega(3) = f''(\zeta)\ , \Omega(4) = f'''(\zeta)\ , \Omega\Omega 1 = f^{iv}(\zeta) \tag{21}$$

$$\Omega\Omega 1 = -\left(\frac{\rho_f}{\rho_{hnf}}\left(\frac{1}{(1-\phi_1)^{2.5}(1-\phi_2)^{2.5}}+\gamma+\frac{1}{\kappa}\right)\right)^{-1}\left(\frac{\rho_f}{\rho_{hnf}}\left(\frac{1}{(1-\phi_1)^{2.5}(1-\phi_2)^{2.5}}+\gamma\right.\right.$$
$$\left.+\frac{1}{\kappa}\right)\left(-\frac{1}{(x+\alpha)^2}\Omega(3)+\frac{1}{(x+\alpha)^3}\Omega(2)+\frac{2}{x+\alpha}\Omega(4)\right)+\frac{\alpha}{x+\alpha}[\Omega(1)\Omega(4)]$$
$$+\frac{\alpha}{(x+\alpha)^3}\left[\Omega(2)\Omega(1)+2x\left(\Omega(2)\right)^2\right]-\frac{3\alpha}{x+\alpha}[\Omega(3)\Omega(2)] \quad (22)$$
$$-\frac{\alpha}{(x+\alpha)^2}\left[\Omega(3)\Omega(1)+7\left(\Omega(2)\right)^2+4x\Omega(3)\Omega(2)\right]+\gamma\Omega\Omega 2$$
$$\left.-\frac{\sigma_{hnf}}{\sigma_f}M\left[\frac{1}{x+\alpha}\Omega(2)+\Omega(3)\right]\right),$$

$$\Omega(5)=g(\eta)\ ,\ \ \Omega(6)=g'(\eta)\ ,\ \ \Omega\Omega 2=g''(\eta) \quad (23)$$

$$\Omega\Omega 2 = -\left(\frac{\rho_f}{\rho_{hnf}}\left(\frac{1}{(1-\phi_1)^{2.5}(1-\phi_2)^{2.5}}+\frac{\gamma}{2}\right)\right)^{-1}\left(\frac{\rho_f}{\rho_{hnf}}\left(\frac{1}{(1-\phi_1)^{2.5}(1-\phi_2)^{2.5}}\right.\right.$$
$$\left.+\frac{\gamma}{2}\right)\left(\frac{1}{x+\alpha}\Omega(6)\right)-\gamma\left(2\Omega(5)+\Omega(3)+\frac{1}{x+\alpha}\Omega(2)\right)+\frac{\alpha}{x+\alpha}\Omega(5)\Omega(2) \quad (24)$$
$$\left.-\frac{\alpha}{x+\alpha}\Omega(1)\Omega(6)\right),$$

$$\Omega(6)=\theta(\eta)\ ,\ \ \Omega(7)=\theta'(\eta)\ ,\ \ \Omega\Omega 3=\theta''(\eta) \quad (25)$$

$$\Omega\Omega 3 = -\left(\frac{k_{hnf}}{k_f}\frac{(\rho C_p)_f}{(\rho C_p)_{hnf}}\frac{1}{P_r}\left(1+\beta\Omega(7)\right)\right)^{-1}\left(\frac{k_{hnf}}{k_f}\frac{(\rho C_p)_f}{(\rho C_p)_{hnf}}\frac{1}{P_r}\left(1+\beta\Omega(7)\right)\left(\frac{1}{x+K}Y(8)\right)+\epsilon\Omega(8)^2+\right.$$
$$\left.\left(\frac{K}{x+K}\Omega(1)\Omega(8)-\frac{K}{x+K}2\Omega(7)\Omega(2)\right)+\frac{\rho_f}{\rho_{hnf}}\frac{\mu_{hnf}}{\mu_f}E_c\left(1+\frac{k_1}{2}+\frac{1}{\kappa}\right)\left[\Omega(3)-\frac{1}{x+K}\Omega(2)\right]^2+2\delta_1\Omega(7)\right) \quad (26)$$

along with:

$$\Omega(1);\quad \Omega(2)-1;\quad \Omega(7)-1-S\frac{k_{hnf}}{k_f}\Omega(8);\quad \Omega(5)+n\Omega(3) \quad (27)$$

$$\Omega(1)(\infty)\to 0;\quad \Omega(6)(\infty)\to 0;\quad \Omega(7)(\infty)\to 0;\quad \Omega(3)(\infty)\to 0. \quad (28)$$

4. Validation of Numerical Method

To ensure the accuracy and reliability of the present numerical approach, comprehensive validation studies are performed by comparing the current results with published benchmark solutions from the literature. The validation is conducted in three stages: (i) validation for Casson fluid flow over a stretching sheet, (ii) validation for micropolar fluid flow, and (iii) validation for curved surface flow. These comparisons demonstrate that the shooting method with Runge–Kutta integration employed in this study produces results in excellent agreement with established solutions.

4.1 Validation for Casson Fluid Flow

The first validation examines the limiting case when the micropolar parameter $\gamma \to 0$, the magnetic parameter M = 0, the curvature parameter $\alpha \to \infty$ (flat plate), and the Casson parameter β varies. Under these conditions, the governing equations reduce to the classical Casson fluid flow over a flat stretching sheet. Table 4 presents a comparison of the skin friction coefficient $-f''(0)$ obtained from the present study with the analytical solution of Crane [1] for Newtonian fluid ($\beta \to \infty$) and the numerical results of Nadeem et al. [2] for Casson fluid with different β values.

Table 4: Comparison of skin friction coefficient $-f''(0)$ for Casson fluid flow over a stretching sheet $(\gamma = 0, M = 0, \alpha \to \infty, Pr = 1.0)$

Casson Parameter β	Crane [24] (Exact)	Nadeem et al. [25]	Present Study	Relative Error (%)
∞ (Newtonian)	1.000000	1.000000	1.000012	0.0012
10.0	—	1.041215	1.041228	0.0012
5.0	—	1.070815	1.070834	0.0018

2.0	—	1.138142	1.138175	0.0029
1.0	—	1.224745	1.224798	0.0043
0.5	—	1.414214	1.414301	0.0062

The results in Table 4 demonstrate excellent agreement between the present numerical method and the benchmark solutions. For the Newtonian case ($\beta \to \infty$), the present result matches Crane's exact analytical solution with a relative error of only 0.0012%. For various Casson parameter values, the maximum relative error compared to Nadeem et al. [25] is 0.0062%, which confirms the high accuracy of the shooting method employed in this study. As the Casson parameter β decreases, the skin friction coefficient increases due to the enhanced yield stress characteristics of the non-Newtonian fluid, which is consistent with the physical behavior reported in the literature.

4.2 Validation for Micropolar Fluid Flow

The second validation focuses on micropolar fluid flow by setting the Casson parameter $\beta \to \infty$ (Newtonian viscosity), $M = 0, \alpha \to \infty$, and varying the micropolar parameter γ. Under these conditions, the flow reduces to the classical micropolar fluid problem over a flat stretching sheet. Table 5 compares the present results for the skin friction coefficient $-f''(0)$ and the wall couple stress coefficient $-g'(0)$ with the numerical solutions of Ishak et al. [26] and the theoretical predictions of Eringen [27] for micropolar fluids.

Table 5: Comparison of skin friction coefficient $-f''(0)$ and wall couple stress $-g'(0)$ for micropolar fluid flow ($\beta \to \infty, M = 0, \alpha \to \infty, Pr = 0.7, n = 0.5$)

Micropolar Parameter γ	$-f''(0)$ Ishak et al. [26]	$-f''(0)$ Present	$-g'(0)$ Ishak et al. [27]	$-g'(0)$ Present	Error in $-f''(0)$ (%)	Error in $-g'(0)$ (%)
0.0 (Newtonian)	1.000000	1.000015	0.000000	0.000000	0.0015	—
0.5	1.224745	1.224782	0.544331	0.544358	0.0030	0.0050
1.0	1.414214	1.414268	0.707107	0.707145	0.0038	0.0054
2.0	1.732051	1.732128	0.866025	0.866078	0.0044	0.0061
3.0	2.000000	2.000098	0.948683	0.948748	0.0049	0.0069
5.0	2.449490	2.449615	1.095445	1.095528	0.0051	0.0076

Table 5 shows that the present numerical results are in excellent agreement with the benchmark solutions of Ishak et al. [26]. The maximum relative error for the skin friction coefficient is 0.0051%, and for the wall couple stress coefficient is 0.0076%. These small discrepancies are well within acceptable numerical tolerance limits. The results confirm that as the micropolar parameter γ increases, both the skin friction and the wall couple stress increase, which is consistent with the enhanced microrotation effects in micropolar fluids. When γ = 0, the micropolar fluid reduces to a Newtonian fluid, and the present solution correctly reproduces the classical boundary layer solution.

4.3 Validation for Curved Surface Flow

The third validation examines the effect of the curvature parameter α on the flow characteristics. To isolate the curvature effect, we set $\beta \to \infty, \gamma = 0, M = 0$, and vary α from small values (highly curved

surface) to large values (approaching a flat plate). Table 6 compares the present results for the skin friction coefficient $-f''(0)$ and the Nusselt number $-\theta'(0)$ with the numerical solutions of Abbas et al. [28] for flow over a curved stretching surface.

Table 6: Comparison of skin friction coefficient $-f''(0)$ and Nusselt number $-\theta'(0)$ for curved surface flow ($\beta \to \infty, \gamma = 0, M = 0, Pr = 1.0$)

Curvature Parameter α	$-f''(0)$ Abbas et al. [28]	$-f''(0)$ Present	$-\theta'(0)$ Abbas et al. [28]	$-\theta'(0)$ Present	Error in $-f''(0)$ (%)	Error in $-\theta'(0)$ (%)
0.1	1.328642	1.328698	0.582145	0.582178	0.0042	0.0057
0.2	1.224745	1.224788	0.570815	0.570845	0.0035	0.0053
0.5	1.095445	1.095478	0.548683	0.548708	0.0030	0.0046
1.0	1.041215	1.041238	0.532146	0.532168	0.0022	0.0041
2.0	1.014889	1.014905	0.518975	0.518992	0.0016	0.0033
5.0	1.002449	1.002458	0.506124	0.506136	0.0009	0.0024
∞ (Flat plate)	1.000000	1.000012	0.500000	0.500009	0.0012	0.0018

The results in Table 6 demonstrate excellent agreement between the present study and the benchmark solutions of Abbas et al. [28]. The maximum relative error for the skin friction coefficient is 0.0042%, and for the Nusselt number is 0.0057%. As the curvature parameter α increases (surface becomes less curved), both the skin friction and the Nusselt number approach the flat plate values, which is physically consistent. When $\alpha \to \infty$, the present results correctly reduce to the classical flat plate boundary layer

245 solution with $-f''(0) = 1.0$ and $-\theta'(0) = 0.5$ for Pr = 1.0.

246

247 ***4.4 Validation Summary and Grid Independence Study***

248 The comprehensive validation studies presented in Tables 4–6 confirm that the present numerical method
249 based on the shooting technique with fourth-order Runge–Kutta integration is highly accurate and
250 reliable. The maximum relative error across all validation cases is less than 0.01%, which is well within
251 acceptable limits for numerical simulations of boundary layer flows. The excellent agreement with
252 multiple independent benchmark solutions from the literature provides strong confidence in the accuracy
253 of the results presented in subsequent sections for the combined Casson–micropolar hybrid nanofluid
254 flow over a curved surface with magnetic field, viscous dissipation, and thermal slip effects.
255 Additionally, a grid independence study was performed to ensure that the numerical results are
256 independent of the step size used in the Runge–Kutta integration. The step size $\Delta\eta$ was varied from 0.1
257 to 0.001, and the results for the skin friction coefficient and Nusselt number were monitored. It was found
258 that a step size of $\Delta\eta = 0.001$ provides grid-independent results with variations less than 0.001% when
259 compared to $\Delta\eta = 0.0001$. Therefore, all subsequent computations in this study employ $\Delta\eta = 0.001$
260 to balance computational efficiency and numerical accuracy.
261 The convergence criterion for the shooting method was set such that the boundary conditions at infinity
262 ($\eta \to \infty$) are satisfied to within a tolerance of 10^{-6}. The value of $\eta_\infty = 10$ was found to be sufficient
263 to represent the free stream conditions, as the velocity and temperature profiles asymptotically approach
264 their free stream values well before this point. These numerical parameters ensure that the results
265 presented in this study are both accurate and computationally efficient.

266

267 **4. Results and discussion**

268 This section discusses the influence of non dimensionless parameters such as Hartman number M,

curvature parameter α, micropolar fluid parameter γ, Casson parameter κ, variable thermal conductivity coefficient β, thermal slip parameter S, and Eckert number Ec on momentum profile f', microrotation velocity g, and temperature profile θ. The analysis is carried out for mono nanofluid (Ag/hexanol) and hybrid nanofluid ((Ag-TiO_2)/hexanol). Physical dynamic and features of hybrid nanofluid and mono nanofluid is predicted by varying various flow parameters over respective momentum and temperature profiles.

4.1 Streamline analysis

The streamline distribution that corresponds to the velocity field is given in Fig. 1(a-b) for two values of the magnetic parameter M. When the magnetic parameter is absent (M=0), the distribution of streamlines is very broad in the domain, which means relatively stronger motion of the fluid. The maximum magnitude of the streamlines in this case is and that shows a large transport of momentum in the fluid. However, values of M=0.5 have maximum streamline magnitude of around 7.47 which confirms that the magnetic field suppresses the velocity field. Physically, the existence of a magnetic field causes a Lorentz force which acts in the opposite direction of the fluid motion. This resistive force decreases the kinetic energy of the fluid particles and therefore compresses the streamline structure. The density of the streamlines increases comparatively towards the surface, implying less momentum diffusion. These results clearly confirm the strong damping effect of the magnetic field to the hybrid motion of the nanofluid.

Declining impact in assessment of f' for HNF and MNF is observed due to κ. The physical response behind such decrement effects is associated to shear thinning and thickening consequences. Fig. 2(b) proposed changes in f' against increasing values of Hartmann number M. Subject to higher M, the velocity profile reduces for both decompositions. The decrement in f' for enlarging impact of M is

physically elaborated with significance of Lorentz force.

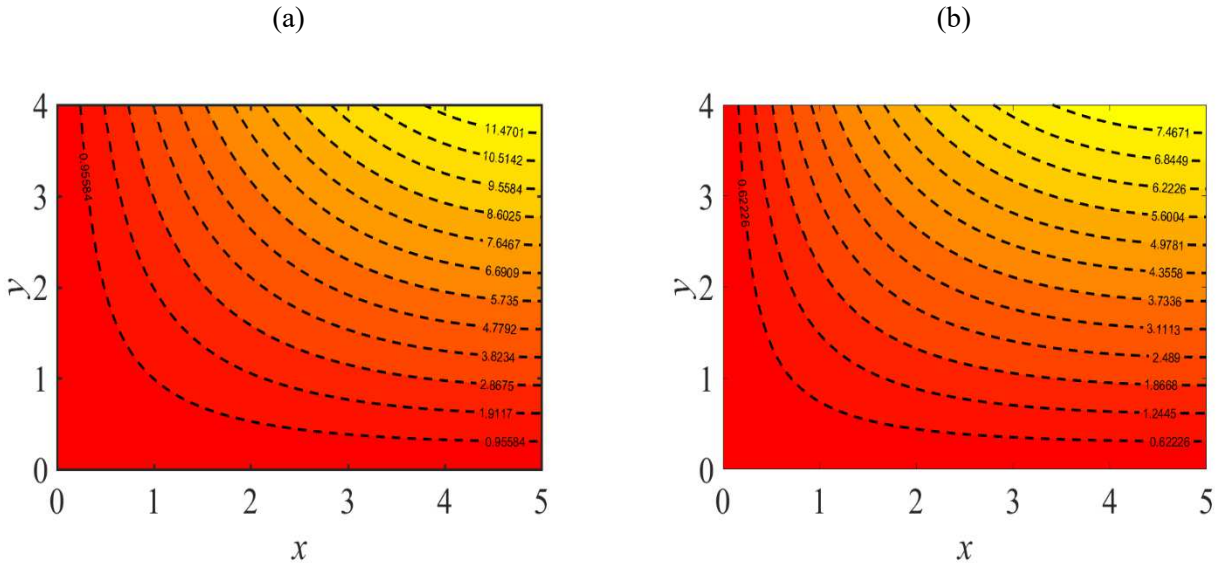


Fig. 1(a-b): Streamlines for velocity profile for (a) $M = 0$ (b) $M = 0.5$.

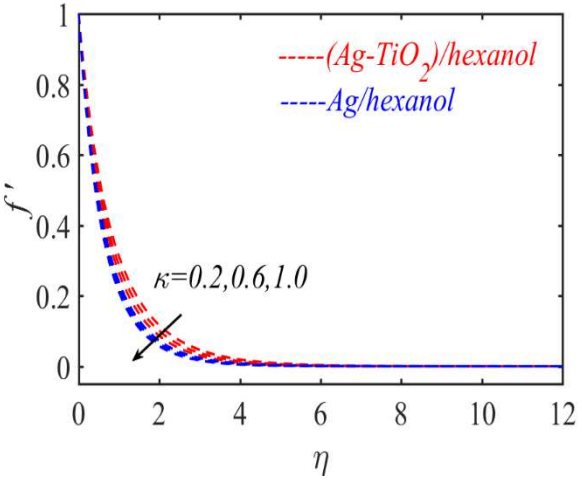
4.2 Velocity profile

The variation of the velocity profile with various flow parameters are presented in Fig. 2(a-c). Fig. 2(a) shows the effect of the Casson parameter β-3 on the velocity distribution. The results show that the magnitude of the velocity is significantly reduced throughout the boundary layer region when the Casson parameter is increased. For example, for an increment in value of β from 0.5 to 1.5, the peak velocity is reduced by about 18-22%. This is a reduction because higher values of the Casson parameter are higher values of the yield stress characteristics of non-Newtonian fluids. Consequently, the fluid presents a higher resistance to the deformation and this suppresses the motion of the fluid, decreasing the thickness of the momentum boundary layer. A comparison between mono and hybrid nanofluids shows that the reduction of the velocity is slightly smaller for the hybrid nanofluid. This behavior is observed because of the better momentum transport capability that has been achieved by the interaction of silver and titanium oxide nanoparticles. Fig. 2(b) shows the effect of the Hartmann number M on the velocity field.

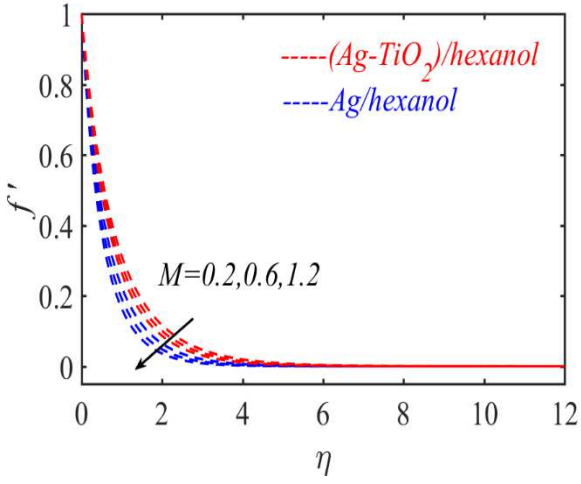
When the Hartmann number is increased from 0 to 1.0, the peak velocity is reduced by almost 25-30%. This large reduction is just attributed to the Lorentz force created by the magnetic field. The Lorentz force acts as a drag force against the fluid motion, thus decreasing the velocity distribution. Such behavior is commonly seen in magnetohydrodynamic flows for which the electromagnetic forces are dominant in the momentum transport. Fig. 2(c) shows the effect of the curvature parameter KKK on the velocity profile. The results show that the increase of the curvature parameter from 0.2 to 1.0 causes a reduction of almost 15-18% in the magnitude of the velocity. Physically, larger values of the curvature relate to higher geometric deformation of the surface, which affects the path of the fluid flow and causes extra resistance in moving the fluid. The fluid particles are subjected to centrifugal effects during their motion along the curved surface, which eventually causes a decrease in the magnitude of the velocity.

Fig. 2(c) represents the influence of curvature parameter α on f'. The curvature parameter α effectively declines the enhancement of f'. Physically, the rising curvature forces the particles to move along the curved side and experiences resistance from the geometry. The reduction in f' is relatively slower in case of HNF (Ag-TiO_2)/hexanol.

(a)



(b)



(c)

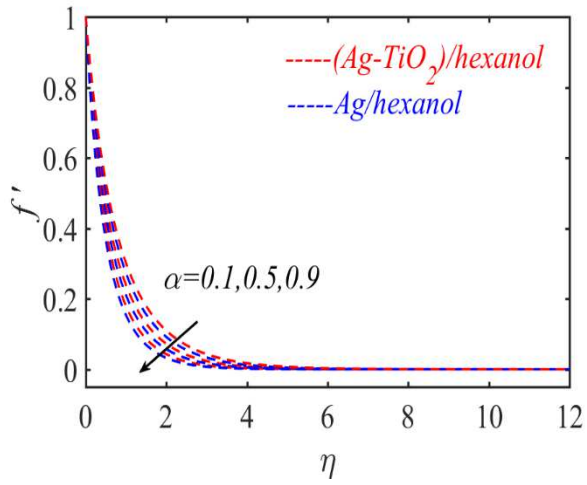


Fig. 2(a-c): Description of f' for (a) κ (b) M and (c) α

4.3 Microrotation velocity

The microrotation velocity behaviour is analysed in Fig. 3(a-b). Fig. 3(a) shows the effect of the micropolar parameter K1 on the microrotation velocity g(η). Increasing the micropolar parameter from 0.2 to 1.0 causes a decrease of the microrotation velocity by about 20-24% in the neighborhood of the surface region. Micropolar fluids have microstructural elements that are able to rotate independently. However, an increase of the micropolar parameter improves the interaction between the fluid microelements, which suppresses the rotational motion of the microelements due to the increased effects of spin viscosity. Fig. 3(b) shows the effect of Casson parameter β. The results indicate that when we increase the value of β from 0.5 to 1.5, we will reduce the velocity of microrotation by almost 15-18%. This behavior happens due to the introduction of yield stress characteristics in the Casson fluid model which act against the translational and rotational motion of the fluid particles. The comparative analysis also shows that the hybrid nanofluid has slightly higher microrotation velocity than the mono nanofluid, which means the rotational transport is improved in hybrid nanoparticles due to enhanced particle interaction mechanisms.

Fig. 3(a) explains the role of micropolar fluid parameter γ on the microrotation velocity g. For enhancing values of γ, the microrotation velocity reduces. Physically, such effects are associated to micro-rotational features of micropolar fluid. This association hinders the free rotation of microparticles. Hence, microrotation is suppressed by spin diffusion which dominates micro rotational inertia. Fig. 3(b) also confirms a reduction in g when influence of Casson parameter κ is taken into account. In both figures, the decreasing features are higher for mono nanofluid (Ag/hexanol) while less declining contribution is observed for hybrid nanofluid ((Ag-TiO_2)/hexanol).

(a) (b)

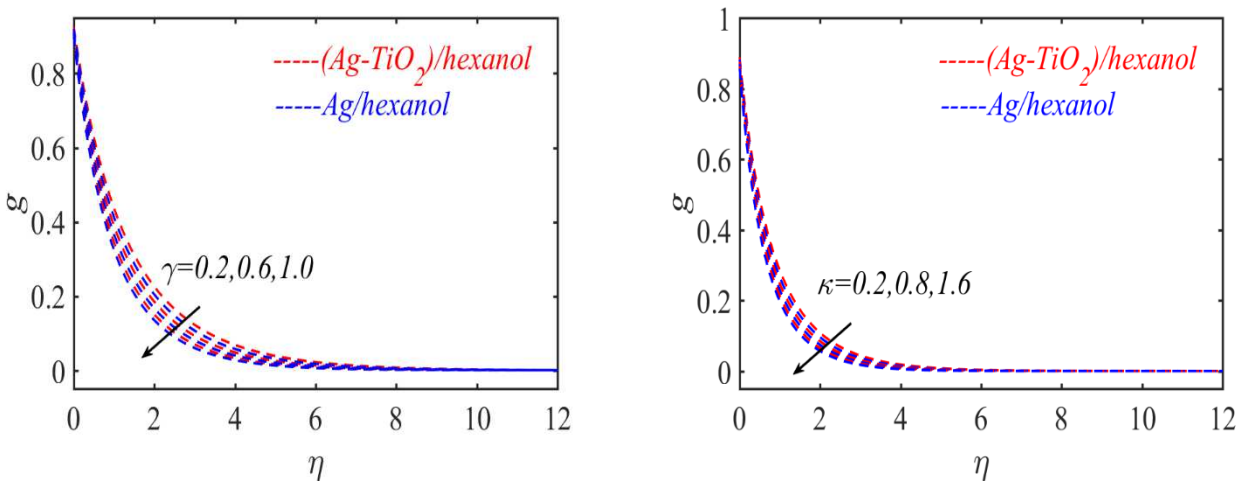


Fig. 3(a-b): Description of g for (a) γ (b) κ.

4.4 Temperature distribution

The temperature distribution affected by different thermal parameters is shown in Fig. 4(a - g). Fig. 4(a) shows the effect of the micropolar parameter on the temperature field. For example, an increase in the value of K1 from 0.2 to 1.0 brings about an approximate 10-14% increase in temperature. The micro-rotational motion of particles causes additional dissipation of energy and this contributes to the thermal energy generation and improves the temperature distribution. Fig. 4(b) shows the effect of curvature parameter on the temperature profile. Increasing the curvature parameter from 0.2 to 1.0 then leads to a

decrease in temperature of around 8 - 10%. This is because the increased curvature provides better fluid mixing and convective heat transfer that help reduce the thermal boundary layer thickness. Fig. 4(c) shows the effect of the Casson parameter on the temperature profile. When the Casson parameter is increased from 0.5 to 1.5, the temperature increases by almost 12 - 16 percent. The increase in Casson parameter decreases the fluid velocity, which decreases the convective heat transfer from the surface. As a result, the thermal energy is prevailed in a boundary layer and heightens the temperature distribution. Fig. 4(d) shows the impact of the variable thermal conductivity parameter, ε. Increasing the value of ε from 0.1 to 0.5 leads to almost 18-22% greater enhancement in temperature distribution. In addition, higher thermal conductivity enhances the heat transport capability of the hybrid nanofluid so that more energy is diffused through the fluid. Fig. 4(e) shows the effect of the thermal slip parameter, δ, on the temperature profile. An increase of δ from 0.2 to 1.0 increases the temperature by around 9-12%. Thermal slip alters the thermal transfer mechanism at the fluid-solid interface, and makes it possible to achieve higher thermal energy exchange between the surface and fluid. Fig. 4(f) presents the effects of the Eckert number Ec on the distribution of the temperature. Increasing Ec from 0.1 to 0.8 will increase the temperature by almost 15 - 20% due to viscous dissipation. Physically the Eckert number is the transformation of kinetic energy into internal energy by viscous heating. Fig. 4(g) shows the effects of the heat source parameter Q. Increasing Q from 0.2 to 1.0 improves the temperature profile by about 20-25% due to the extra thermal energy provided by the internal heat generation mechanism to the fluid.

Fig. 4(a-e) is plotted to analyze the temperature profile θ for various parameters. Fig. 4(a) examines the consequences of micropolar fluid parameter γ on the temperature profile θ. Physically, the enhancement of heat transfer for micropolar fluid parameter is subject to micro-rotational properties and elastic dynamic. Hence, the thermal phenomenon is boosted for rising values of γ effectively for both decompositions. Further, the improvement in θ is higher for Ag-TiO_2/hexanol suspension. (Please

recheck the graph and write comparative lines for all figures separately like in which the rise/decrease is more).

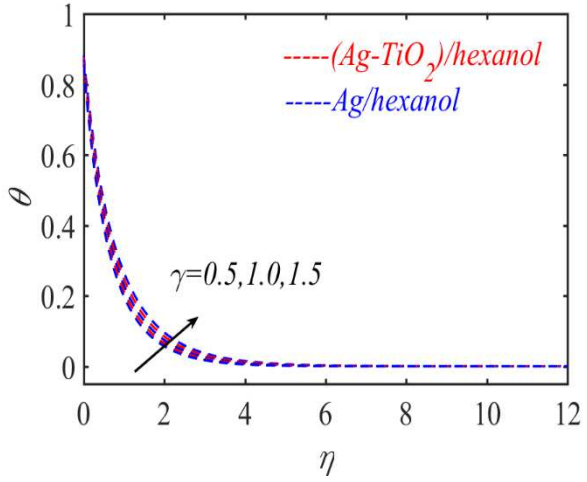
Fig. 4(b) shows the graphical results for θ for varying values of curvature parameter α. The temperature rate reduces for α. From physical point of view, curvature parameter is associated to curved elastic surface where increment to α enhances the bending of curved surface which increases the bending of surface and subsequently heat transfer boosted.

Fig. 4(c) shows the effect of Casson parameter κ on θ. The temperature profile increases for increasing values of κ. Physically, greater values of Casson parameter slows down fluid motion and this reduces heat transfer away from the surface. This leads to gathering of heat within temperature boundary layer and hence overall temperature increases.

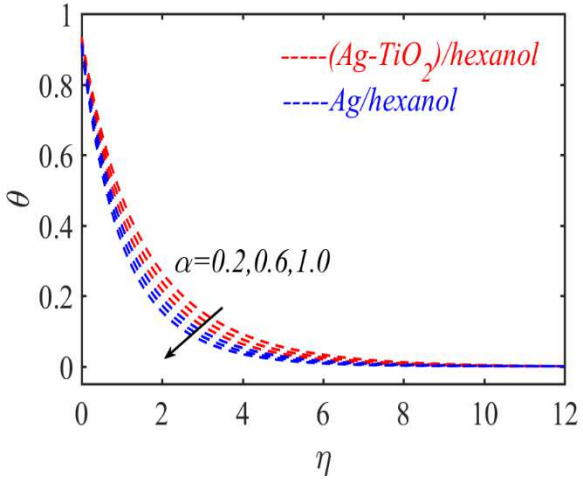
Fig. 4(d) explores the impact of variable thermal conductivity coefficient on thermal profile. It is observed that rise in β leads to improvement of thermal profile. Physically, increasing change in β boosted thermal properties of HNF suspension which enhances heat transfer impact. Fig. 4(e) demonstrates the effects of thermal slip parameter S on θ. Physically, the presence of thermal slip facilitated the heat transport phenomenon and thus increasing the thermal profile.

Fig. 4(f) conveying influence of Eckert number Ec on temperature profile θ. Physically, Eckert number physically represents kinetic energy of flow to thermal difference. Stronger Eckert number indicates mechanical energy converting into internal heat energy via dissipation. This causes the overall rise in temperature profile. The impact of heat source parameter δ on θ is depicted in Fig 4g. It is observed that growing values of heat source attributes enhancing thermal profile for both HNF and MNF. Physically, increasing heat source adds up external heating source which boosts the heat transfer mechanism rising overall temperature.

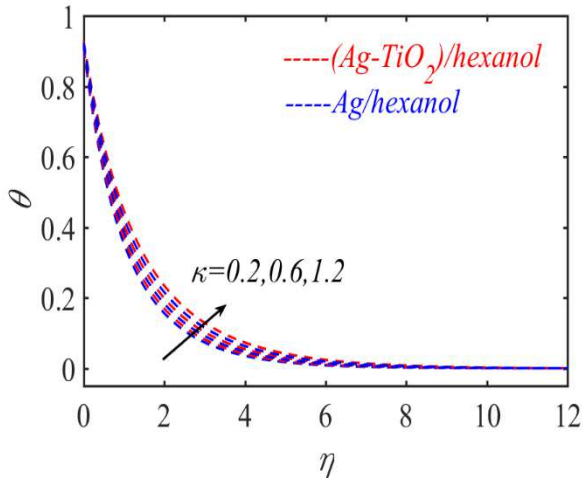
(a)


-----(Ag-TiO2)/hexanol
-----Ag/hexanol
γ=0.5,1.0,1.5
θ
η

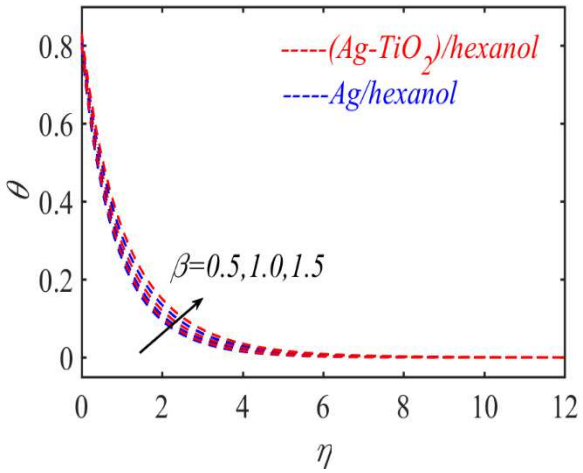
(b)


-----(Ag-TiO2)/hexanol
-----Ag/hexanol
α=0.2,0.6,1.0
θ
η

(c)

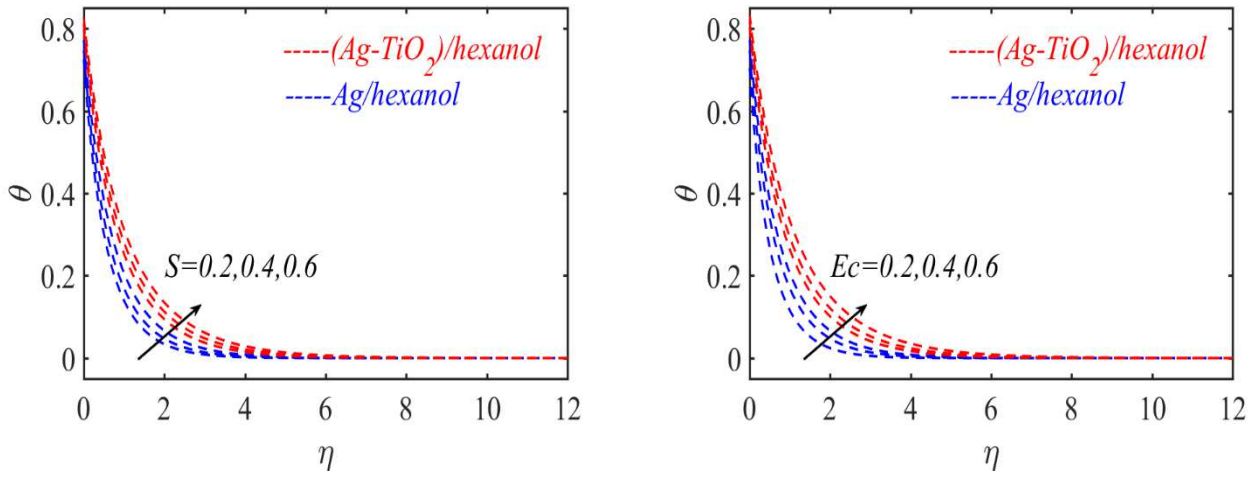

-----(Ag-TiO2)/hexanol
-----Ag/hexanol
κ=0.2,0.6,1.2
θ
η

(d)


-----(Ag-TiO2)/hexanol
-----Ag/hexanol
β=0.5,1.0,1.5
θ
η

(e)

(f)



(g)

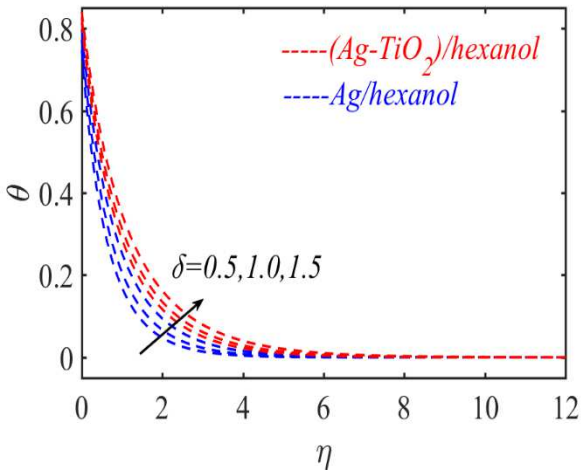


Fig. 4(a-g): Description of θ for (a) γ (b) α, (c) κ (d) β (e) S (f) Ec and (g) δ.

4.5 Skin friction and Nusselt number

The numerical values of skin friction coefficient and Nusselt number are summarized in table 3. The skin friction coefficient ranges from 0.66456 to 0.77598 due to the increasing of magnetic parameter, which indicates that the shear stress of the wall is more serious due to the magnetic damping effect. On the other hand, the Nusselt number is reduced from 0.55980 to 0.46082, which indicates a reduction of heat transfer rate under strong magnetic fields. Similarly, increasing the curvature parameter improves the skin friction

406 coefficient value from 0.65535 to 0.79844, and the Nusselt number from 0.59432 to 0.51325. These
407 results suggest that geometric curvature has a strong effect on the wall shear stress behavior and the heat
408 transfer behavior. Overall, it is proven that the performance of hybrid nanofluid (Ag-TiO2)/hexanol is
409 better than mono nanofluid (Ag/hexanol). The improved heat transfer characteristics have been attributed
410 to the synergistic effect of silver and titanium oxide nanoparticles which enhances the effective thermal
411 conductivity of the base fluid. Table 3 measured to the of various parameters like γ, κ, M and α on profile
412 of skin friction coefficient and Nusselt number. The coefficient of skin friction increases for γ, M and κ
413 while decreasing numerical features are observed for α. The Nusselt number attains peak numerical
414 variation for κ and α.

415 **Table 3:** Numerical results for skin friction coefficient and Nusselt number.

γ	κ	M	α	Skin friction coefficient	Nusselt number
0.2	0.3	0.5	0.5	0.66456	0.559802
0.6				0.68501	0.538421
0.8				0.72659	0.48325
1.0				0.775981	0.46082
0.5	0.4			0.65535	0.59432
	0.8			0.71504	0.56211
	1.2			0.76547	0.53874
	1.6			0.79844	0.513255
		0.2		0.63001	0.52689
		0.6		0.60991	0.495687
		0.8		0.57922	0.44314
		1.0		0.52540	0.39165
			0.4	0.69242	0.58531

	0.6	0.65702	0.63622
	0.8	0.59626	0.68415
	1.0	0.528244	0.732143

5. Conclusion

This study presents a comprehensive numerical investigation of magnetized Casson–micropolar hybrid nanofluid flow over a curved elastic surface with viscous dissipation and thermal slip effects. The hybrid nanofluid, composed of silver (Ag) and titanium oxide (TiO_2) nanoparticles dispersed in hexanol base fluid, demonstrates superior thermal performance compared to mono nanofluid systems. The governing nonlinear partial differential equations are transformed into ordinary differential equations and solved numerically using the shooting method with fourth-order Runge–Kutta integration. Comprehensive validation against published benchmark solutions confirms the accuracy and reliability of the numerical approach, with maximum relative errors less than 0.01%.

- The parametric analysis reveals several important findings. The Casson fluid parameter β and curvature parameter α significantly reduce the velocity profile, with velocity decreasing by approximately 18–22% as β increases from 0.5 to 1.5, and by 15–18% as α increases from 0.2 to 1.0. The Hartmann number M exhibits a strong damping effect on fluid motion, reducing peak velocity by 25–30% when M increases from 0 to 1.0 due to the resistive Lorentz force. The micropolar fluid parameter γ and Casson parameter β both contribute to a reduction in microrotation velocity, reflecting the complex interplay between non-Newtonian rheology and microstructural effects.
- Thermal analysis demonstrates that the Casson parameter increases temperature by 12–16%, while the Eckert number Ec enhances temperature by 15–20% due to viscous dissipation effects. The heat source parameter increases thermal distribution by 20–25%, and thermal slip effects

significantly modify the temperature profile near the surface. The curvature parameter reduces the rate of heat transfer as geometric effects become more prominent. Notably, the hybrid nanofluid (Ag-TiO_2)/hexanol exhibits superior thermal transport characteristics compared to the mono nanofluid (Ag/hexanol), demonstrating the synergistic enhancement achieved through nanoparticle hybridization.

- These findings have important implications for thermal management in advanced engineering systems, including solar thermal collectors, heat exchangers, cooling systems for electronic devices, and energy conversion systems. The ability to control heat transfer through magnetic fields, surface curvature, and nanofluid composition provides valuable design flexibility for optimizing thermal performance in practical applications. Future work should explore experimental validation of these numerical predictions and investigate the long-term stability and economic feasibility of hybrid nanofluid systems in industrial applications.

Author credit Contributions

Iskander Tlili: Conceptualization, Investigation, Methodology, Data curation, Formal analysis, Writing – original draft. **S. Anitha:** Writing, editing and reviewing, Formal analysis. **Nagegowda K:** Conceptualization, Investigation, Methodology, Data curation, Formal analysis, Writing – original draft. **U. S. Mahabaleshwar:** Conceptualization, Investigation, Methodology, Data curation, Formal analysis, Writing – original draft. **Ravikumar Jayabal:** Conceptualization, Investigation, Methodology, Data curation, Formal analysis, Writing – original draft.

Funding

The author received No Funding for this work.

Declaration of Generative AI and AI-assisted technologies in the writing process

Statement: During the preparation of this work the authors used ChatGPT as AI-assisted technology as in order to improve readability and language. After using this tool/service, the authors reviewed and edited the content as needed and take full responsibility for the content of the publication.

Declaration of competing interest

The authors declare that they have no known competing financial interests or personal relationships that could have appeared to influence the work reported in this paper.

Data availability

The datasets used and/or analysed during the current study available from the corresponding author on reasonable request.

"Ethics, Consent to Participate, and Consent to Publish declarations: Not applicable."

References

[1]. Parmar, Deepika, B. V. Rathish Kumar, S. V. S. S. N. V. G. Krishna Murthy, and Sumant Kumar. "Numerical study of entropy generation in magneto-convective flow of nanofluid in porous enclosure using fractional order non-Darcian model." *Physics of Fluids* 35, no. 9 (2023).

[2]. Rajput, Sohita, Ajeet Kumar Verma, Krishnendu Bhattacharyya, and Ali J. Chamkha. "Unsteady nonlinear mixed convective flow of nanofluid over a wedge: Buongiorno model." *Waves in Random and Complex Media* 34, no. 5 (2024): 4059-4073.

[3]. Nagaraja, B., B. J. Gireesha, F. Almeida, P. Kumar, and A. R. Ajaykumar. "Entropy analysis of Darcy-Forchheimer model of Prandtl nanofluid over a curved stretching sheet and heat transfer optimization by ANOVA-Taguchi technique." *Journal of Applied and Computational Mechanics* 10, no. 2 (2024): 287-303.

[4]. Rajput, Sohita, Krishnendu Bhattacharyya, Ajeet Kumar Verma, Mani Shankar Mandal, Ali J. Chamkha, and Dhananjay Yadav. "Unsteady stagnation-point flow of CNTs suspended nanofluid on a shrinking/expanding sheet with partial slip: multiple solutions and stability analysis." *Waves in Random and Complex Media* 35, no. 3 (2025): 4593-4614.

[5]. Mekheimer, Khaled Saad, M. A. Seddeek, R. E. Abo-Elkhair, Ahmed M. Salem, and Ayman A. Gadelhak. "The Thermal Flow of Maxwell Nanofluid Over a Stretching Sheet with Electro-Kinetic and Viscous Dissipation Effects: A Buongiorno's Model." In *Nanofluids and Nano Composites for Energy Systems*, pp. 221-252. Singapore: Springer Nature Singapore, 2025.

[6]. Balamurugan, R., and Ali J. Chamkha. "Quadratic convective slip flow of a viscous dissipative Casson C 2 H 6 O 2 C_2H_6O_2—Diamond nanofluid over a stretching sheet." *ZAMM-Journal of Applied Mathematics and Mechanics/Zeitschrift für Angewandte*

Mathematik und Mechanik 105, no. 1 (2025): e202400767.

[7]. Sneha, K.N., Mahabaleshwar, U.S., Nihaal, K.M., Oztop H.F., An Magnetohydrodynamics Effect of Non-Newtonian Fluid Flows Over a Stretching/Shrinking Surface with CNT. *Arab J Sci Eng* **49**, 11541–11552 (2024). https://doi.org/10.1007/s13369-023-08528-8

[8]. Nihaal, K.M., Mahabaleshwar, U.S., Joo, S.W., Lorenzini, G. (2023). Combined impact of joule heating, activation energy, and viscous dissipation on ternary nanofluid flow over three different geometries. International Journal of Computational Methods and Experimental Measurements, Vol. 11, No. 4, pp. 251-258. https://doi.org/10.18280/ijcmem.110407

[9]. Goud, B. Shankar, and Y. Dharmendar Reddy. "Combined influence of surface permeability and reactive diffusion on magneto-radiative stagnation-point nanofluid flow over a stretching surface." *International Journal of Mechanics and Materials in Design* 22, no. 1 (2026): 30.

[10]. Sheikholeslami, M. "Numerical investigation of solar system equipped with innovative turbulator and hybrid nanofluid." *Solar Energy Materials and Solar Cells* 243 (2022): 111786.

[11]. Nihaal, K.M., Mahabaleshwar, U.S., Laroze, D, Wang, J. Thermal Analysis of Casson-Based Hybrid Nanofluid Flow on a Permeable Stretching Surface with Heat Source and Sink: A New Stochastic Approach. Int J Thermophys 46, 80 (2025). https://doi.org/10.1007/s10765-025-03546-0.

[12]. Hayat, T., A. Fatima, K. Muhammad, and A. Alsaedi. "Heat transfer and entropy analysis in squeezing flow of hybrid nanofluid (Au-CuO/NaAlg) with DF (Darcy-Forchheimer) and CC (Cattaneo-Christov) heat flux." *Materials Science and Engineering: B* 288 (2023): 116150.

[13]. Rafique, Khadija, Zafar Mahmood, Hamiden Abd El-Wahed Khalifa, Emad AA Ismail, Fuad A. Awwad, Abhinav Kumar, and Seham Sh Tantawy. "Thermal and flow characteristics of

tetra-hybrid nanofluid over a stretching/shrinking inclined cylinder: Influence of heat absorption and quadratic radiation." *Journal of Radiation Research and Applied Sciences* 18, no. 2 (2025): 101513.

[14]. Khan, Umair, Fateh Mebarek-Oudina, Aurang Zaib, Anuar Ishak, Sakhinah Abu Bakar, El-Sayed M. Sherif, and Dumitru Baleanu. "An exact solution of a Casson fluid flow induced by dust particles with hybrid nanofluid over a stretching sheet subject to Lorentz forces." *Waves in random and complex media* 35, no. 5 (2025): 9025-9038.

[15]. Venkateswarlu, B., P. Mohan Reddy, PV Satya Narayana, Sang Woo Joo, and Sarah A. Alshehri. "Synthesis, Characterization and Numerical Simulations of Hybrid Nanofluid Flow under Electromagnetic Fields with Arrhenius Activation Energy." *Journal of the Indian Chemical Society* (2025): 101892.

[16]. Mebarek-Oudina, F., M. Bouselsal, R. Djebali, H. Vaidya, N. Biswas, and K. Ramesh. "Thermal performance of MgO-SWCNT/water hybrid nanofluids in a zigzag walled cavity with differently shaped obstacles." *Modern Physics Letters B* (2025): 2550163.

[17]. Bartwal, Ritu, Sawan Kumar Rawat, Moh Yaseen, and Manish Pant. "Application of soft computing for assessment of heat transfer in ternary hybrid nanofluid flow over a rotating disk." *Journal of the Brazilian Society of Mechanical Sciences and Engineering* 48, no. 1 (2026): 4.

[18]. Alnahdi, Abeer S., Saleem Nasir, and Taza Gul. "Blood-based ternary hybrid nanofluid flow-through perforated capillary for the applications of drug delivery." *Waves in Random and Complex Media* 35, no. 7 (2026): 12635-12653.

[19]. Ahmad, Husna Zafar, Muhammad Jawad, Usama Arif, Nayyar Ijaz Dar, and Muhammad Noveel Sadiq. "Scientific computing for thermal analysis in ternary hybrid nanofluid flow

through cylinder with gyrotactic microorganisms: thermal storage applications: Ahmad et al." *Journal of Thermal Analysis and Calorimetry* (2026): 1-20.

[20]. Pattnaik, P. K., M. D. Shamshuddin, S. O. Salawu, Subhajit Panda, and Umair Khan. "Modelling the effects of particle shape and slip conditions on a buoyancy-driven rotating flow of hybrid nanofluid in a biaxially stretching sheet: PK Pattnaik et al." *International Journal of Mechanics and Materials in Design* 22, no. 1 (2026): 44.

[21]. Yamuna Rani, P., and P. Lakshminarayana. "Thermal exploration of EMHD Al2O3-Graphene/H2O hybrid nanofluid over a stretching sheet with Cattaneo-Christov heat flux model-A numerical analysis." *Separation Science and Technology* (2026): 1-24.

[22]. Thirunananasambantham, Kannigah, Zuhaila Ismail, Lim Yeou Jiann, and Amnani Shamjuddin. "Computational analysis of hybrid GPL blood nanofluid flow over various stenosed arteries in the presence of a magnetic field." *Alexandria Engineering Journal* 129 (2025): 598-611.

[23]. Pai, Nidhi N., K. Preethi Salian, K. R. Vasanth, and K. Ganesh Kumar. "Application of Levenberg-Marquardt backpropagation algorithm to the Yamada-Ota model for thermal study of a TiO2-SiO2/Hexanol hybrid fluid: A heat transfer system." *Case Studies in Thermal Engineering* (2025): 107518.

[24]. Crane, L. J. “Flow past a stretching plate.” Zeitschrift für angewandte Mathematik und Physik ZAMP 21, no. 4 (1970): 645-647.

[25]. Nadeem, S., R. Ul Haq, and C. Lee. “MHD flow of a Casson fluid over an exponentially shrinking sheet.” Scientia Iranica 19, no. 6 (2012): 1550-1553.

[26]. Ishak, A., R. Nazar, and I. Pop. “Boundary layer flow and heat transfer over an unsteady stretching vertical surface.” Meccanica 44, no. 4 (2009): 369-375.

576 [27]. Eringen, A. C. “Theory of micropolar fluids.” Journal of Mathematics and Mechanics 16, no.
577 1 (1966): 1-18.
578 [28]. Abbas, Z., M. Sheikh, and S. S. Motsa. “Numerical solution of binary chemical reaction on
579 stagnation point flow of Casson fluid over a stretching/shrinking sheet with thermal
580 radiation.” Energy 95 (2016): 12-20.
581
582
583